Quantum mechanics/molecular mechanics simulation of the ligand vibrations of the water-oxidizing Mn_4CaO_5 cluster in photosystem II

Shin Nakamura[a] and Takumi Noguchi[a,1]

[a]Division of Material Science, Graduate School of Science, Nagoya University, Nagoya 464-8602, Japan

During photosynthesis, the light-driven oxidation of water performed by photosystem II (PSII) provides electrons necessary to fix CO_2, in turn supporting life on Earth by liberating molecular oxygen. Recent high-resolution X-ray images of PSII show that the water-oxidizing center (WOC) is composed of an Mn_4CaO_5 cluster with six carboxylate, one imidazole, and four water ligands. FTIR difference spectroscopy has shown significant structural changes of the WOC during the S-state cycle of water oxidation, especially within carboxylate groups. However, the roles that these carboxylate groups play in water oxidation as well as how they should be properly assigned in spectra are unresolved. In this study, we performed a normal mode analysis of the WOC using the quantum mechanics/molecular mechanics (QM/MM) method to simulate FTIR difference spectra on the S_1 to S_2 transition in the carboxylate stretching region. By evaluating WOC models with different oxidation and protonation states, we determined that models of high-oxidation states, $Mn(III)_2Mn(IV)_2$, satisfactorily reproduced experimental spectra from intact and Ca-depleted PSII compared with low-oxidation models. It is further suggested that the carboxylate groups bridging Ca and Mn ions within this center tune the reactivity of water ligands bound to Ca by shifting charge via their π conjugation.

photosynthesis | water oxidation | QM/MM | FTIR | carboxylate ligand

The oxidation of water, performed by photosystem II (PSII) in plants and cyanobacteria, is a crucial part of the photosynthesis process, providing a source of electrons used for CO_2 fixation. This process also produces molecular oxygen as a byproduct; this "waste" oxygen is released to the atmosphere, where it plays an essential role in sustaining life on Earth. The catalytic site of water oxidation is a water-oxidizing center (WOC) located in the electron-donor side of PSII (1–3). Recent high-resolution (1.9–1.95 Å) X-ray crystallographic structures of PSII (4, 5) revealed that the WOC core is an Mn_4CaO_5 cluster fixed to the protein by six carboxylate [D1-D170, D1-E189, D1-E333, D1-D342, D1-A344 (C terminus), and CP43-E354] ligands and one imidazole (D1-H332) ligand. Four water ligands are also bound to Mn_4 (W1 and W2) and Ca (W3 and W4) (Fig. 1B shows numbering of the Mn ions and water ligands); several water molecules also exist around the Mn_4CaO_5 cluster, forming a hydrogen bond network (Fig. 1A). Because of the absence of the information of hydrogen atoms in the X-ray structures, however, the protonation states of the water and oxo ligands in Mn_4CaO_5 as well as the structure of the hydrogen bond network remain to be clarified.

The water-oxidizing reaction proceeds through a cycle of five intermediates designated as S_n states ($n = 0$–4) (6, 7), where S_1 is the most stable in the dark. Oxidation of the Mn_4CaO_5 cluster by a $Y_Z^\bullet$ radical, produced by light-induced charge separation, advances the S_n state ($n = 0$–3) to the S_{n+1} state. The S_4 state immediately relaxes to the S_0 state on release of O_2. The oxidation states of the Mn atoms within the cluster have long been a source of debate, especially around whether the cluster exists in a high-oxidation [$Mn(III)_2Mn(IV)_2$] or low-oxidation [$Mn(III)_4$ or $Mn(II)Mn(III)_2Mn(IV)$] state in S_1 (8–12).

With the information of atomic coordinates from high-resolution X-ray structures of the WOC, quantum chemical calculation is now a very powerful method in investigation of the water oxidation mechanism (10, 12–24). Calculations using the density functional theory (DFT) and quantum mechanics/molecular mechanics (QM/MM) methods can be used to predict individual S-state structures and hence, the reaction scheme. Experimental data, such as EPR and extended X-ray absorption fine structure (EXAFS), as well as X-ray structural information were simulated using these methods to identify the protonation structure and the oxidation states (10, 13, 15, 20, 21), although a definite conclusion has not yet been reached. In contrast to EPR and EXAFS, which provide information mainly about the Mn_4CaO_5 core, FTIR spectroscopy provides structural information about the protein moiety and water molecules coupled to the Mn_4CaO_5 cluster (25–27). FTIR spectroscopy, which detects molecular vibrations, is highly sensitive to the structures and interactions of functional groups, and hence, the FTIR difference technique can recognize subtle structural changes at a much finer structural resolution than X-ray crystallography. Flash-induced FTIR difference spectra taken during the S-state cycle show many prominent signals in the protein region. In particular, characteristic features were observed around 1,400 cm^{-1} in the region of the symmetric stretching vibrations of carboxylate groups (28–35). Such signals reflect significant changes in the interactions of carboxylate groups around the Mn_4CaO_5 cluster, implying that these carboxylate groups are deeply involved in the water oxidation mechanism. The observation that Ca^{2+} depletion drastically changed the spectral feature around 1,400 cm^{-1} (28, 36) also supports this idea. Thus, analyzing the structural changes of

Significance

Photosystem II plays an important role in photosynthesis by oxidizing water; this process provides as an electron source to fix CO_2 during photosynthesis, which sustains life on Earth by liberating molecular oxygen. Although the catalytic site, the water-oxidizing center (WOC), is known to consist of an Mn_4CaO_5 cluster, six carboxylate ligands, and one imidazole ligand, its detailed structure and reaction mechanism have not yet been resolved. In this study, we successfully simulated the carboxylate stretching region of the experimental IR spectra of WOC by calculating WOC vibrations using the quantum mechanics/molecular mechanics method. Our simulations show the significant role that carboxylate groups bridging Mn and Ca play in tuning the water oxidation reaction.
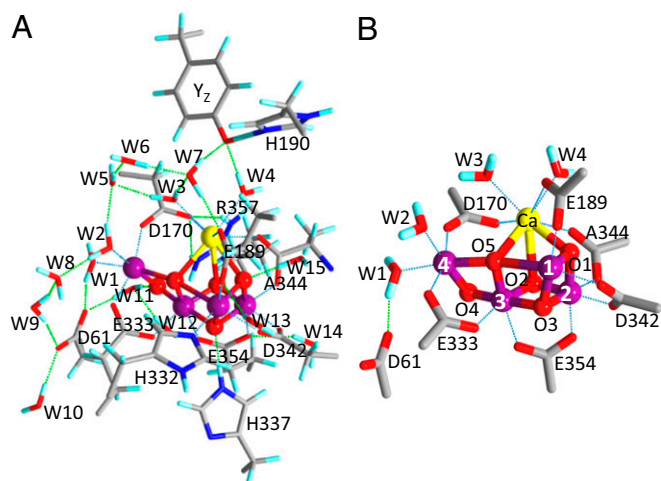
Fig. 1. (A) Optimized structure of the whole QM region in the QM/MM calculation of WOC (model 1, S_1 state). E354 and R357 are on the CP43 protein, and other residues are on the D1 protein. Blue, N; cyan, H; gray, C; purple, Mn; red, O; yellow, Ca. (B) Carboxylate groups and water ligands around the Mn_4CaO_5 cluster with numbering of Mn and oxygen atoms.

carboxylate groups during the S-state cycle provides crucial information regarding the mechanism of this reaction. However, clear assignment of the FTIR bands to individual carboxylate groups has not been achieved, except for the C-terminal carboxylate of D1-Ala344, which has bands that were assigned successfully by its selective labeling with [1-^{13}C]Ala (31, 32).

In this study, the carboxylate stretching region of the FTIR difference spectra of the WOC was simulated using QM/MM calculations, which were based on a damage-free X-ray structure obtained using an X-ray free electron laser (XFEL) (5). Several WOC models with different oxidation and protonation states (Table 1) were assumed to reproduce the experimental S_2/S_1 difference (30) and ^{12}C/^{13}C-Ala S_2/S_1 double-difference (31) spectra. The S_2/S_1 difference spectrum of a Ca-depleted WOC (28) was also simulated. These FTIR spectra show subtle changes in bond lengths and interactions of carboxylate groups, thus providing a different way of evaluating the most accurate WOC model from previous simulations using EXAFS and EPR data (10, 13, 15, 20, 21). This QM/MM simulation provides sufficient reproduction of the FTIR spectra, showing the significance of carboxylate ligands in the water oxidation mechanism.

Results

The quantum mechanics (QM) region of the WOC (Fig. 1A) used in QM/MM calculations (see Fig. S1 for the whole QM/MM region) included six carboxylate ligands (D170, E189, E333, D342, E354, and A344; subunit names are omitted hereafter) and one nearby carboxylate group (D61) hydrogen bonded with W1 (Fig. 1B). All of the amino acid groups and water molecules interacting with these carboxylate groups were included in the QM region to accurately reproduce carboxylate vibrations. Different protonation states at W2 and O5 as well as high- and low-oxidation states of the Mn ions were assumed in the constructed models (Table 1). Model 1 (W2/O5 = H_2O/O^{2-}) and model 2 (W2/O5 = OH^-/O^{2-}), which both have high-oxidation states, have been used in many previous DFT and QM/MM studies (10, 14, 16, 18–20, 22), whereas model 3 (W2/O5 = OH^-/H_2O) and model 4 (W2/O5 = H_2O/OH^-) have low-oxidation states that previous DFT calculations suggested could fit to the 1.9- and 1.95-Å structures, respectively, revealed by X-ray crystallography (12). A model of a Ca-depleted WOC with the same protonation and oxidation states as model 1 was also calculated (model 5) (Fig. S2). In the S_2 state, Mn_1 or Mn_4 was

oxidized in the high-oxidation models, whereas Mn_2 or Mn_4 was oxidized in the low-oxidation models. The Mn_1- and Mn_4-oxidized S_2 states of the high-oxidation models have been proposed to reflect two conformations showing $g = 4.1$ and $g = 2$ multiline EPR signals, respectively, where the latter conformation has a slightly lower energy (10, 14, 17).

The optimized Mn_4CaO_5 cluster geometries, specifically metal–metal, metal–O, metal–water (O), and metal–ligand (O or N) distances, together with deviations from the XFEL X-ray structure (5) are summarized in Table S1. Models 1 and 2 showed relatively small deviations (rmsd = 0.12–0.13 Å), whereas models 3 and 4 showed larger deviations (rmsd = 0.25 and 0.15 Å, respectively). In particular, model 3 has very large deviations in Mn_3-O5 and Mn_4-O5 (0.93 and 0.86 Å, respectively). The calculated distances of model 1 are very similar to those in previous QM/MM calculations (18, 19). A relatively large deviation of Mn_3-O5 (−0.44 Å) from the XFEL structure could be attributed to a minor contribution of the S_0 state as previously suggested (20). IR spectra of the WOC were simulated within the symmetric COO^- stretching region at around 1,400 cm^{-1}. This region does not overlap with other vibrational modes in contrast to a severe overlap of the strong amide II bands in the asymmetric COO^- region around 1,550 cm^{-1} (29). Simulated S_2/S_1 IR difference spectra of model 1 agreed well with the experimental spectrum (30) for both of the S_2 states oxidized at Mn_1 and Mn_4 (Fig. 2 A, a). In particular, the prominent negative band present at 1,401 cm^{-1} with positive bands on both the higher- and lower-frequency sides of this peak was well-reproduced. The ^{12}C/^{13}C-Ala S_2/S_1 double-difference spectra calculated using model 1, with both the Mn_1- and Mn_4-oxidized S_2 sates, also well-reproduced the experimental spectrum obtained in the work by Chu et al. (31), which showed major bands at 1,356(−)/1,339(+)/1,320(+)/1,302(−) representing the vibrations of the C-terminal carboxylate of D1-A344 (Fig. 2 B, a). The calculated spectra of model 2, with the S_2 states oxidized at Mn_1 and Mn_4, also showed features similar to those of the experimental S_2/S_1 difference spectrum (Fig. 2 A, b) and are in good agreement with the ^{12}C/^{13}C-Ala S_2/S_1 double-difference spectrum (Fig. 2 B, b). In contrast to high-oxidation models, the low-oxidation models, 3 and 4, poorly reproduced the S_2/S_1 difference spectrum (Fig. 2 A, c and d). The ^{12}C/^{13}C-Ala S_2/S_1 difference spectrum was also not reproduced by model 3 (Fig. 2 B, c), although model 4 reproduced major features of the ^{12}C/^{13}C-A344 difference spectrum (Fig. 2 B, d).

The calculated normal modes of symmetric COO^- vibrations of model 1 in the S_1 and Mn_4-oxidized S_2 states are depicted under the simulated S_2/S_1 spectrum in Fig. 3A (normal modes of other high-oxidation models are shown in Fig. S3, and assignments are summarized in Tables S2 and S3). Most of the COO^- vibrations show significant couplings among carboxylate groups, although lower-frequency bands at 1,350–1,250 cm^{-1} arise from isolated vibrations of A344 and E189, which bridge Mn and Ca ions. It is notable that the prominent negative band at 1,401 cm^{-1} arises mainly from the isolated vibration of D170 in model 1 (Fig. 3A and Fig. S3A). The vibration of E333 also contributes to the lower-frequency side of the band. In the S_2 state, these vibrations are downshifted to ~1,360 cm^{-1}. The bands at 1,436/1,418 cm^{-1} may

Table 1. Mn_4CaO_5 cluster models used for QM/MM calculations

Model	Oxidation states in S_1*	W2	O5	Oxidized Mn in S_2
1	High (III, IV, IV, III)	H_2O	O^{2-}	Mn_1 or Mn_4
2	High (III, IV, IV, III)	OH^-	O^{2-}	Mn_1 or Mn_4
3	Low (III, III, III, III)	OH^-	H_2O	Mn_2
4	Low (III, IV, III, II)	H_2O	OH^-	Mn_4
5 (Ca depleted)	High (III, IV, IV, III)	H_2O	O^{2-}	Mn_4

*Oxidation states of (Mn_1, Mn_2, Mn_3, Mn_4).

Nakamura and Noguchi
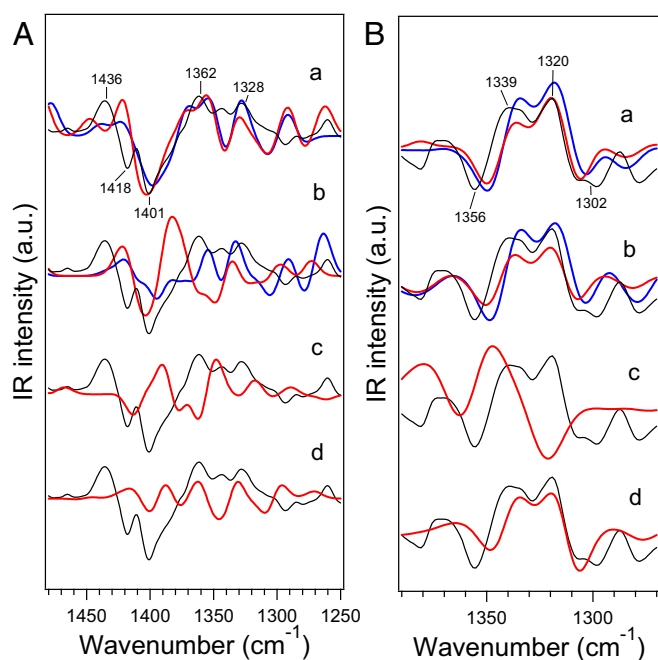
Fig. 2. Calculated IR spectra in the symmetric COO⁻ stretching vibrations of carboxylate groups (red or blue lines) compared with experimental FTIR difference spectra (black lines). (A) S_2/S_1 difference spectra. (B) $^{12}C/^{13}C$-A344 S_2/S_1 double-difference spectra. (a) Model 1 (blue line, Mn_1-oxidized S_2; red line, Mn_4-oxidized S_2), (b) model 2 (blue line, Mn_1-oxidized S_2; red line, Mn_4-oxidized S_2), (c) model 3, and (d) model 4. Experimental spectra in A and B were taken from refs. 30 and 31, respectively.

be assigned to the vibrations of D61, D342, and E189 calculated at 1,450–1,420/~1,410 cm⁻¹ (Fig. 3A and Fig. S3A); the deviations from the experimental frequencies may be because of slightly different scaling factors depending on the vibrational modes. The same tendency was also found in model 2 (Fig. S3 B and C). In this case, however, E333 is the main vibration for the 1,401-cm⁻¹ band, whereas D170 contributes to the higher-frequency band together with D61 and D342. Thus, deprotonation of W2 induces a slight rearrangement of COO⁻ vibrations without drastic changes in their frequencies (SI Text has detailed discussion about the effect of W2 deprotonation).

Downshifts in frequencies associated with D170 and E333 are consistent with changes in CO lengths within COO⁻ (Table 2); the CO bond interacting with Mn_4 has a longer length than the other CO bond interacting with Ca (D170) or Mn_3 (E333) in the S_1 state, and the former CO further lengthens on S_2 formation, whereas the latter CO is shortened. This asymmetric structure weakens the coupling of two CO vibrations within the COO⁻ group. This change in the coupling increases the contribution of the longer CO bond in the "symmetric" COO⁻ stretching vibration, resulting in observed frequency downshifts. The CO length changes in D170 and E333 are induced by stronger interactions with Mn_4 as shown in the tendency toward shortened distances of D170-Mn_4 and E333-Mn_4 (Table S1) on S_2 formation.

Normal modes in the simulated $^{12}C/^{13}C$-Ala S_2/S_1 double-difference spectrum are shown in Fig. 3B for model 1 with an Mn_4-oxidized S_2 state. It is clear that the major experimental bands at 1,356/1,339/1,320/1,302 cm⁻¹ arise from ^{13}C-induced shifts of isolated A344 vibrations at 1,356(S_1)/1,339(S_2) cm⁻¹ to 1,320(S_1)/1,302(S_2) cm⁻¹ by 36–37 cm⁻¹. The relatively low frequency of the A344 vibration and the 17-cm⁻¹ downshift on S_2 formation are consistent with its asymmetric structure and an increased asymmetry on S_2 formation; it has longer (1.294-Å) and shorter (1.236-Å) CO bonds on the Mn_2 and Ca sides,

respectively, which change by +0.0005 and −0.0001 Å, respectively (Table S1). Weak coordination to Ca is reflected in the distance of A344-Ca (2.54 Å), which is long relative to A344-Mn_2 (1.91 Å), in good agreement with experimental values (2.43 and 1.90 Å, respectively) (Table S1). This weak coordination to Ca is also consistent with experimental observations that the A344 bands are insensitive to the replacement of Ca^{2+} with Sr^{2+} (32). Similar trends in vibrational frequencies and bond lengths within A344 are also found in other high-oxidation models (Fig. S3, Table 2, and Table S1).

A simulated S_2/S_1 difference spectrum of the Ca-depleted WOC (model 5), which is shown in Fig. 4 with band assignments, is in good agreement with the experimental spectrum (28). In particular, the isolated D170 vibration at ~1,400 cm⁻¹ in the intact WOC (Fig. 3A) is downshifted to ~1,350 cm⁻¹, and a positive feature around 1,360 cm⁻¹ arising from the coupled D170 vibrations is lost. These alterations are consistent with a change from bidentate to unidentate coordination on Ca^{2+} removal, which is reflected in variations in CO lengths (specifically, +0.024 and −0.030 Å on the Mn_4 and free sides, respectively) (Table 2). Vibrations of other carboxylate groups are also rearranged significantly on Ca^{2+} depletion (Fig. 4).
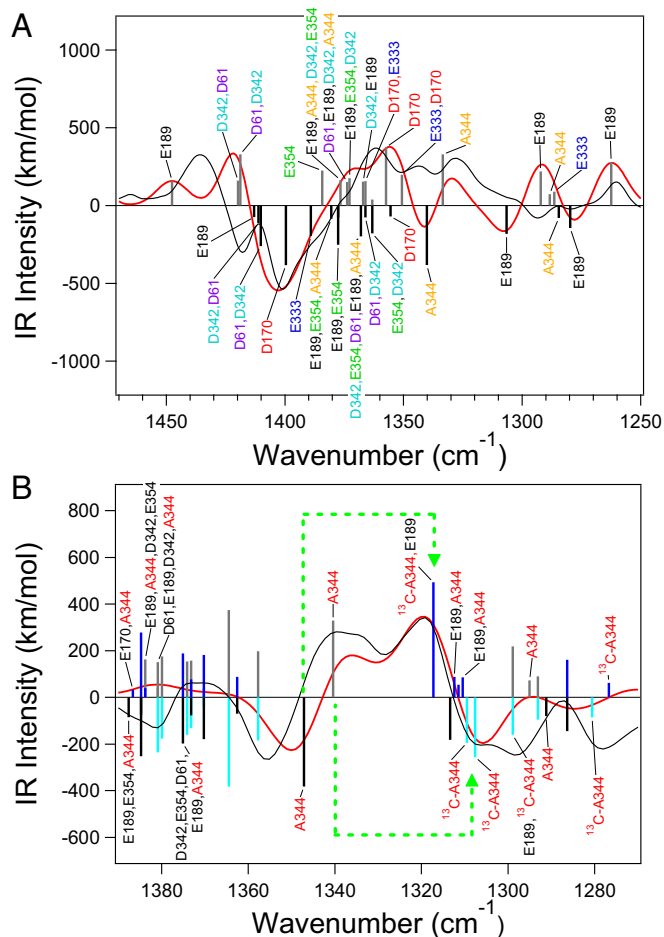
Fig. 3. Assignments of the symmetric COO⁻ stretching vibrations of model 1 in the S_1 and Mn_4-oxidized S_2 states. (A) S_2/S_1 difference spectrum. (B) $^{12}C/^{13}C$-A344 S_2/S_1 double-difference spectrum. Calculated normal modes of unlabeled WOC are expressed as black (S_1) and gray (S_2) bars, whereas those of [1-^{13}C]Ala-WOC are expressed as blue (S_1) and cyan (S_2) bars. Calculated and experimental (30, 31) spectra are shown as red and black lines, respectively. In B, [1-^{13}C]Ala–induced shifts of calculated major A344 modes are indicated by green dotted arrows.

Table 2. CO bond lengths (angstroms) of carboxylate groups calculated for high-oxidation models

Carboxylate*	Model 1			Model 2			Model 5 (Ca depleted)	
	Length (Å)	ΔS_2 (Mn$_1$)[†]	ΔS_2 (Mn$_4$)[†]	Length (Å)	ΔS_2 (Mn$_1$)[†]	ΔS_2 (Mn$_4$)[†]	Length (Å)	ΔS_2 (Mn$_4$)[†]
D170(Mn$_4$)	1.271	+0.012	+0.015	1.257	+0.009	+0.019	1.294	+0.025
D170(Ca)	1.265	−0.005	−0.008	1.280	−0.004	−0.013	1.235	−0.009
E189(Mn$_1$)	1.295	+0.009	+0.006	1.297	+0.006	+0.005	1.295	+0.008
E189(Ca)	1.248	−0.003	−0.001	1.244	0.000	0.000	1.236	−0.003
E333(Mn$_3$)	1.266	−0.003	−0.008	1.272	0.000	−0.012	1.262	−0.007
E333(Mn$_4$)	1.277	+0.012	+0.014	1.266	+0.008	+0.017	1.276	+0.013
D342(Mn$_1$)	1.261	+0.014	+0.007	1.260	+0.012	+0.004	1.259	+0.002
D342(Mn$_2$)	1.272	−0.004	−0.002	1.271	−0.004	−0.002	1.269	−0.001
E354(Mn$_2$)	1.287	+0.001	−0.010	1.289	+0.001	−0.008	1.279	−0.008
E354(Mn$_3$)	1.263	+0.006	+0.013	1.258	+0.005	+0.010	1.264	+0.011
A344(Mn$_2$)	1.294	+0.009	+0.005	1.292	+0.009	+0.005	1.304	+0.004
A344(Ca)	1.236	−0.003	−0.001	1.235	−0.004	−0.001	1.225	−0.001
D61(W1)	1.268	+0.011	+0.007	1.263	+0.009	+0.009	1.260	+0.008
D61(W9)	1.262	−0.005	+0.002	1.264	−0.004	−0.006	1.265	−0.004

*Interacting metal or water is in parentheses.
[†]Change in length by formation of the S$_2$ state. Oxidized Mn is indicated in parentheses.

Discussion

A number of theoretical simulations of the Mn$_4$CaO$_5$ cluster have been attempted to clarify details regarding its structure and physical properties. Most of these simulations focused on the geometry and the spin properties of the Mn$_4$CaO$_5$ cluster to reproduce the X-ray structure as well as EXAFS and EPR data (10, 13, 15, 20, 21). In a recent study, Chuah et al. (23) performed DFT calculations on the Mn$_4$CaO$_5$ cluster with its first-shell ligands to outline how carboxylate stretching frequencies behave on Mn oxidation and deprotonation. In this study, we present a successful simulation of the FTIR difference spectra of the WOC in the carboxylate stretching region; to do this simulation, we performed QM/MM calculations with a large QM region including nearby amino acids and water molecules in addition to first-shell ligands (Fig. 1A).

Our calculations satisfactorily reproduced the symmetric COO⁻ stretching region of the experimental S$_2$/S$_1$ difference spectrum (30) by using high-oxidation models (models 1 and 2), which have an oxidation state of (III, IV, IV, III) in the S$_1$ state (Fig. 2 A, a and b). Model 1 showed a slightly better reproduction compared with model 2. Both of the high-oxidation models also showed a good reproduction of the ¹²C/¹³C-A344 S$_2$/S$_1$ double-difference spectrum (31) (Fig. 2 B, a and b), which specifically represents the A344 (C-terminal carboxylate) bands. This result indicates that the A344 vibrations in the S$_1$ and S$_2$ states are estimated correctly by calculations. In addition, the Ca-depleted model (model 5) showed a good agreement with the experimental S$_2$/S$_1$ difference spectrum of Ca-depleted PSII (28) (Fig. 4). These successful reproductions of experimental spectra lend credibility to the QM/MM calculations and proposed assignments of prominent spectral features (Figs. 3 and 4).

In contrast to the high-oxidation models, both of the low-oxidation models (models 3 and 4) (Table 1) did not reproduce the S$_2$/S$_1$ difference spectrum (Fig. 2 A, c and d). In addition, the ¹²C/¹³C-Ala difference spectrum was not reproduced by model 3, although the major spectral feature was reproduced by model 4 (Fig. 2 B, c and d). Thus, low-oxidation models previously used to reproduce X-ray structures (12) are unlikely according to carboxylate vibrations. Previous DFT simulations of EXAFS and EPR data also support this conclusion (10).

The QM region used in vibrational analysis includes six carboxylate ligands surrounding the Mn$_4$CaO$_5$ cluster and the D61 hydrogen bonded to W1. The result that simulations with this QM region reproduced the experimental FTIR difference spectra in

the COO⁻ stretching region indicates that the COO⁻ bands in the spectra originate mostly from these seven carboxylate groups closely interacting with the Mn$_4$CaO$_5$ cluster. The vibrations of these carboxylate groups are coupled significantly with each other in most normal modes (Fig. 3A). On formation of S$_2$, carboxylate groups are rearranged without drastic changes in coordination, resulting in frequency shifts and alteration in couplings shown in the simulated S$_2$/S$_1$ difference spectrum (Fig. 3A). Because strong couplings exist among carboxylate groups alongside charge delocalization (Table S4), we conclude that virtually all of the carboxylate groups contribute to the experimental spectrum (Fig. 3A). Among the normal modes, D170 and E333, ligands bound to Mn$_4$, have rather isolated vibrations at ~1,400 cm⁻¹ in S$_1$, which change to coupled vibrations at ~1,360 cm⁻¹ on S$_2$ formation, providing prominent bands at these positions in the difference spectrum (Fig. 3A). In addition, the calculated Mulliken charges (Table S4) show that an additional charge is distributed largely to Mn$_4$ when not only Mn$_4$ is oxidized but also, Mn$_1$ is formally oxidized on S$_2$ formation. This increased charge at Mn$_4$ induces frequency downshifts of carboxylate ligands. Thus, this charge
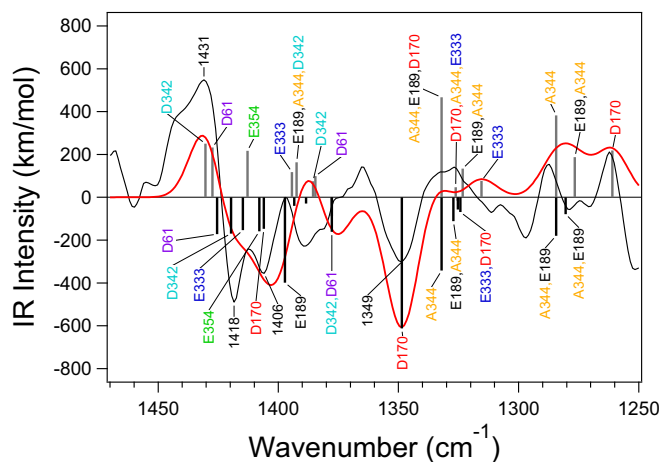
Fig. 4. A calculated S$_2$/S$_1$ IR difference spectrum in the symmetric COO⁻ stretching region of the Ca-depleted WOC model (model 5; red line) compared with the experimental FTIR difference spectrum of Ca-depleted PSII (black line). Calculated normal modes are expressed as black (S$_1$) and gray (S$_2$) bars. The experimental spectrum was taken from ref. 28.

distribution to Mn$_4$ explains the major contribution of the Mn$_4$ ligands (D170 and E333) to the spectral feature and further explains the unexpected similarity between the calculated spectra with Mn$_1$- and Mn$_4$-oxidized S$_2$ states (Fig. 2 *A*, *a*). Large changes in Mn$_4$ ligands are consistent with a recent QM/MM analysis of the S$_2$ − S$_1$ difference Fourier map from XFEL X-ray diffraction data (37), which suggests that the main structural change during the S$_1$→S$_2$ transition is in the position of Mn$_4$ and its coordination environment (38). Krewald et al. (10) also suggested that the S$_1$→S$_2$ transition should mostly affect the D170 and E333 vibrations because of Mn$_4$(III)'s loss of Jahn–Teller axis on oxidation. The experimental observation that the prominent negative band at ~1,400 cm^{-1} is lost on Ca^{2+} depletion (28, 36) is also consistent with the assignment of this band to D170 bridging Mn$_4$ and Ca; the spectral change is well-explained in calculation of the Ca-depleted WOC (model 5), in which the D170 vibration downshifts to ~1,350 cm^{-1} because of a change from bidentate to unidentate coordination (Fig. 4). Assigning the ~1,400-cm^{-1} band to a carboxylate bridge between Mn and Ca was previously proposed from this FTIR observation (28).

Site-directed mutagenesis of cyanobacteria has been used to investigate how carboxylate amino acid residues are involved in COO$^-$ vibrations of FTIR difference spectra of S-state transitions (33–35, 39–47). In contrast to selective isotope labeling using [1-^{13}C]A344 (31, 32), the effects of mutation on FTIR spectra are not straightforward because of the full or partial inactivation of the WOC on mutation of critical residues, secondary effects on WOC structure, and rearrangement of vibrational couplings of carboxylate groups. On E354Q mutation, the S$_2$/S$_1$ FTIR difference spectrum showed intensity changes in the 1,440- to 1,300-cm^{-1} region, which spans virtually the entire symmetric COO$^-$ region (33, 34). Because the E354 vibration contributes to coupled modes over the 1,390- to 1,360-cm^{-1} range in calculated spectra (Fig. 3*A*), experimental alterations may be explained by rearrangements in the ligand structure and changes in vibrational couplings that occur in addition to the loss of E354 vibrations. In addition, D61A mutation induced changes in the 1,440- to 1,410-cm^{-1} and 1,370- to 1,320-cm^{-1} regions of the S$_2$/S$_1$ spectrum (35), which are consistent with major contributions of D61 to coupled modes present at 1,420–1,410 and 1,370–1,360 cm^{-1} (Fig. 3*A*). We note several puzzling observations; specifically, mutations of D170, E189, E333, and D342 induced no or minor changes in the COO$^-$ region in the FTIR difference spectra during the S-state cycle, which is concomitant with little change in oscillation patterns (39–42). These carboxylate ligands are thought to be crucial in supporting the structure of the Mn$_4$CaO$_5$ cluster, where their negative charges should be important in determining the redox potential of S-state intermediates. Thus, it is expected that mutations within these carboxylate groups would significantly affect the WOC structure as well as its reactions. In addition, vibrations of these carboxylate groups are heavily coupled with those of other carboxylate groups (Fig. 3*A*). Thus, mutation of one of the carboxylate groups (even if it is not coordinated to the formally oxidized Mn) should alter vibrational features, resulting in perturbation in the FTIR difference spectra. Indeed, mutations in amino acid residues that are located far from the Mn$_4$CaO$_5$ cluster but interact with it through a hydrogen bond network, such as D2-K317 (43, 44), D1-N181 (45), D1-E65, D2-E312, D1-R334, and D1-Q165 (46, 47), showed clear changes in the COO$^-$ region of the FTIR spectra during the S-state cycle. In most cases, the mutations also lowered the efficiency of the S$_3$→S$_0$ transition. Although recent DFT studies suggested that deprotonation of water/hydroxide ligands coordinating an oxidized Mn suppresses frequency shifts of carboxylate ligands (23, 48), the S$_1$→S$_2$ transition is not accompanied by release of protons (49); additionally, it is not possible that several carboxylate ligands are all silent in any Mn$_4$CaO$_5$ models. Rather, the data in these DFT studies, which showed frequency shifts, to a more or less extent, in virtually all of the carboxylate

ligands (23, 48), are consistent with our results. Additional studies on carboxylate ligands mutants are necessary to resolve discrepancies between the mutational effects on FTIR data and QM/MM calculation results.

We also note a clear trend where D170, A344, and E189, which bridge Mn and Ca, show asymmetric structural changes; this trend includes lengthened CO bonds on the Mn side and shortened CO bonds on the Ca side on S$_2$ formation (Table 2), which result in relatively large frequency downshifts (Fig. 3*A*). This change is caused by an increase in positive charge on Mn ions on S$_2$ formation, which attracts a negative charge on the COO$^-$ group and induces single- and double-bond characters in the CO bonds on Mn and Ca sides, respectively (Mn...O$^-$−C = O...Ca). This shift of negative charge through the conjugated COO$^-$ group from the Ca side to the Mn side eventually increases the positive charge on Ca^{2+} (Table S4), which then increases the acidity of water molecules on Ca (W3 and W4). This alteration in charge on Ca is also reflected in a decrease in Ca-W3 and Ca-W4 distances (Table S1) and an increase in OH lengths in W3 and W4 on S$_2$ formation (Table S5). It is known that replacing Ca^{2+} with Sr^{2+} decreases the water oxidation rate (50), which can be caused by the difference in Lewis acidity between Ca^{2+} and Sr^{2+} (51, 52). It is, thus, possible that the W3 and W4 attached to Ca^{2+} are involved in proton release in water oxidation, especially during the S$_2$→S$_3$ transition, which is inhibited by Ca^{2+} depletion (53). It has also been proposed that W3 moves to Mn$_4$ during the S$_2$→S$_3$ transition in the so-called oxo-oxyl mechanism (13, 17, 22). Thus, the carboxylate ligands bridging Mn and Ca ions may play an important role in water oxidation by tuning the reactivity of water ligands on Ca by charge shifts via their π conjugation.

Methods

The initial coordinates of PSII models were obtained from the XFEL X-ray structure at a resolution of 1.95 Å (5) (Protein Data Bank ID code 4UB6). In addition to the Mn$_4$CaO$_5$ cluster, amino acid residues, water molecules, and two Cl$^-$ ions located within 20 Å from the Mn$_4$CaO$_5$ cluster were extracted from the X-ray structure. Hydrogen atoms were generated and optimized using the AMBER force field (54). During this procedure, the positions of all heavy atoms were fixed. QM/MM calculations were performed using the two-layer ONIOM method (55) with the electronic embedding scheme within the Gaussian 09 program package (56). The QM region (Fig. 1) consists of the Mn$_4$CaO$_5$ cluster, amino acid ligands (D1-D170, D1-E333, D1-D342, D1-A344, CP43-E354, and D1-H332), water ligands (W1, W2, W3, and W4), 11 other water molecules that surround the Mn$_4$CaO$_5$ cluster, Y$_Z$, D1-H190, D1-D61, D1-H337, and CP43-R357. Other atoms in the selected region were assigned to the molecular mechanics (MM) region (Fig. S1). Geometry optimization and normal mode analysis of the QM region were performed using an unrestricted DFT method with the B3LYP functional using LANL2DZ and 6−31G(d) as basis sets for metal atoms and other atoms, respectively (24). In QM/MM geometry optimization, the coordinates of the QM region were fully relaxed, whereas those of the MM region were fixed. Table 1 shows the oxidation and protonation states of calculated models. The oxidation states of (Mn$_1$, Mn$_2$, Mn$_3$, Mn$_4$) in the S$_1$ state are (III, IV, IV, III) in high-oxidation models and (III, III, III, III) or (III, IV, III, II) in low-oxidation models. Mn$_1$ or Mn$_4$ and Mn$_2$ or Mn$_4$ were oxidized on S$_2$ formation in the high- and low-oxidation models, respectively. High-spin states were assumed in calculations. The protonation states of W2 and O5 were assumed to be H$_2$O, OH$^-$, or O^{2-} following previous studies (10, 12–24).

To obtain IR spectra in the COO$^-$ stretching region, normal modes involving carboxylate vibrations were added by assuming a Gaussian band with a 16-cm^{-1} width (FWHM) for each mode. A scaling factor was determined for each simulated difference spectrum (for models 1 and 2, an average spectrum of Mn$_1$- and Mn$_4$-oxidized S$_2$) to adjust the frequency of the simulated major peak to that of the experimental one; this major peak includes the negative peak at 1,401 cm^{-1} in the S$_2$/S$_1$ difference spectrum, the positive peak at 1,320 cm^{-1} in the ^{12}C/^{13}C-Ala S$_2$/S$_1$ double-difference spectrum, and the positive peak at 1,431 cm^{-1} in the S$_2$/S$_1$ difference spectrum of Ca-depleted PSII. Adopted scaling factors ranged from 0.955 to 0.966. When the corresponding peak was not found in a calculated spectrum, a scaling factor of 0.960 was adopted.

1. McEvoy JP, Brudvig GW (2006) Water-splitting chemistry of photosystem II. *Chem Rev* 106(11):4455–4483.
2. Cox N, Messinger J (2013) Reflections on substrate water and dioxygen formation. *Biochim Biophys Acta* 1827(8-9):1020–1030.
3. Yano J, Yachandra V (2014) Mn₄Ca cluster in photosynthesis: Where and how water is oxidized to dioxygen. *Chem Rev* 114(8):4175–4205.
4. Umena Y, Kawakami K, Shen J-R, Kamiya N (2011) Crystal structure of oxygen-evolving photosystem II at a resolution of 1.9 Å. *Nature* 473(7345):55–60.
5. Suga M, et al. (2015) Native structure of photosystem II at 1.95 Å resolution viewed by femtosecond X-ray pulses. *Nature* 517(7532):99–103.
6. Joliot P, Barbieri G, Chabaud R (1969) A new model of photochemical centers in system II. *Photochem Photobiol* 10(5):309–329.
7. Kok B, Forbush B, McGloin M (1970) Cooperation of charges in photosynthetic O₂ evolution-I. A linear four step mechanism. *Photochem Photobiol* 11(6):457–475.
8. Roelofs TA, et al. (1996) Oxidation states of the manganese cluster during the flash-induced S-state cycle of the photosynthetic oxygen-evolving complex. *Proc Natl Acad Sci USA* 93(8):3335–3340.
9. Kulik LV, Epel B, Lubitz W, Messinger J (2007) Electronic structure of the Mn₄OₓCa cluster in the S₀ and S₂ states of the oxygen-evolving complex of photosystem II based on pulse ⁵⁵Mn-ENDOR and EPR spectroscopy. *J Am Chem Soc* 129(44):13421–13435.
10. Krewald V, et al. (2015) Metal oxidation states in biological water splitting. *Chem Sci* 6(3):1676–1695.
11. Zheng M, Dismukes GC (1996) Orbital configuration of the valence electrons, ligand field symmetry, and manganese oxidation states of the photosynthetic water oxidizing complex: Analysis of the S₂ state multiline EPR signals. *Inorg Chem* 35(11):3307–3319.
12. Petrie S, Pace RJ, Stranger R (2015) Resolving the differences between the 1.9 Å and 1.95 Å crystal structures of photosystem II: A single proton relocation defines two tautomeric forms of the water-oxidizing complex. *Angew Chem Int Ed Engl* 54(24):7120–7124.
13. Ames W, et al. (2011) Theoretical evaluation of structural models of the S₂ state in the oxygen evolving complex of Photosystem II: Protonation states and magnetic interactions. *J Am Chem Soc* 133(49):19743–19757.
14. Pantazis DA, Ames W, Cox N, Lubitz W, Neese F (2012) Two interconvertible structures that explain the spectroscopic properties of the oxygen-evolving complex of photosystem II in the S₂ state. *Angew Chem Int Ed Engl* 51(39):9935–9940.
15. Galstyan A, Robertazzi A, Knapp EW (2012) Oxygen-evolving Mn cluster in photosystem II: The protonation pattern and oxidation state in the high-resolution crystal structure. *J Am Chem Soc* 134(17):7442–7449.
16. Siegbahn PEM (2013) Water oxidation mechanism in photosystem II, including oxidations, proton release pathways, O-O bond formation and O₂ release. *Biochim Biophys Acta* 1827(8-9):1003–1019.
17. Bovi D, Narzi D, Guidoni L (2013) The S₃ state of the oxygen-evolving complex of photosystem II explored by QM/MM dynamics: Spin surfaces and metastable states suggest a reaction path towards the S₄ state. *Angew Chem Int Ed Engl* 52(45):11744–11749.
18. Pal R, et al. (2013) S₀-State model of the oxygen-evolving complex of photosystem II. *Biochemistry* 52(44):7703–7706.
19. Saito K, Ishikita H (2014) Influence of the Ca²⁺ ion on the Mn₄Ca conformation and the H-bond network arrangement in Photosystem II. *Biochim Biophys Acta* 1837(1):159–166.
20. Askerka M, Vinyard DJ, Wang J, Brudvig GW, Batista VS (2015) Analysis of the radiation-damage-free X-ray structure of photosystem II in light of EXAFS and QM/MM data. *Biochemistry* 54(9):1713–1716.
21. Li X, Siegbahn PEM, Ryde U (2015) Simulation of the isotropic EXAFS spectra for the S₂ and S₃ structures of the oxygen evolving complex in photosystem II. *Proc Natl Acad Sci USA* 112(13):3979–3984.
22. Shoji M, Isobe H, Yamaguchi K (2015) QM/MM study of the S₂ to S₃ transition reaction in the oxygen-evolving complex of photosystem II. *Chem Phys Lett* 636:172–179.
23. Chuah WY, Stranger R, Pace RJ, Krausz E, Frankcombe TJ (2016) Deprotonation of water/hydroxo ligands in clusters mimicking the water oxidizing complex of PSII and its effect on the vibrational frequencies of ligated carboxylate groups. *J Phys Chem B* 120(3):377–385.
24. Nakamura S, Ota K, Shibuya Y, Noguchi T (2016) Role of a water network around the Mn₄CaO₅ cluster in photosynthetic water oxidation: A Fourier transform infrared spectroscopy and quantum mechanics/molecular mechanics calculation study. *Biochemistry* 55(3):597–607.
25. Chu H-A (2013) Fourier transform infrared difference spectroscopy for studying the molecular mechanism of photosynthetic water oxidation. *Front Plant Sci* 4:146.
26. Debus RJ (2015) FTIR studies of metal ligands, networks of hydrogen bonds, and water molecules near the active site Mn₄CaO₅ cluster in Photosystem II. *Biochim Biophys Acta* 1847(1):19–34.
27. Noguchi T (2015) Fourier transform infrared difference and time-resolved infrared detection of the electron and proton transfer dynamics in photosynthetic water oxidation. *Biochim Biophys Acta* 1847(1):35–45.
28. Noguchi T, Ono T, Inoue Y (1995) Direct detection of a carboxylate bridge between Mn and Ca²⁺ in the photosynthetic oxygen-evolving center by means of Fourier transform infrared spectroscopy. *Biochim Biophys Acta* 1228(2-3):189–200.
29. Noguchi T, Sugiura M (2003) Analysis of flash-induced FTIR difference spectra of the S-state cycle in the photosynthetic water-oxidizing complex by uniform ¹⁵N and ¹³C isotope labeling. *Biochemistry* 42(20):6035–6042.
30. Noguchi T, Sugiura M (2002) Flash-induced FTIR difference spectra of the water oxidizing complex in moderately hydrated photosystem II core films: Effect of hydration extent on S-state transitions. *Biochemistry* 41(7):2322–2330.
31. Chu H-A, Hillier W, Debus RJ; Isotope-edited FTIR study (2004) Evidence that the C-terminus of the D1 polypeptide of photosystem II is ligated to the manganese ion that undergoes oxidation during the S₁ to S₂ transition: An isotope-edited FTIR study. *Biochemistry* 43(11):3152–3166.
32. Strickler MA, Walker LM, Hillier W, Debus RJ (2005) Evidence from biosynthetically incorporated strontium and FTIR difference spectroscopy that the C-terminus of the D1 polypeptide of photosystem II does not ligate calcium. *Biochemistry* 44(24):8571–8577.
33. Shimada Y, et al. (2009) Effect of a single-amino acid substitution of the 43 kDa chlorophyll protein on the oxygen-evolving reaction of the cyanobacterium *Synechocystis* sp. PCC 6803: Analysis of the Glu354Gln mutation. *Biochemistry* 48(26):6095–6103.
34. Service RJ, et al. (2011) Participation of glutamate-354 of the CP43 polypeptide in the ligation of manganese and the binding of substrate water in photosystem II. *Biochemistry* 50(1):63–81.
35. Debus RJ (2014) Evidence from FTIR difference spectroscopy that D1-Asp61 influences the water reactions of the oxygen-evolving Mn₄CaO₅ cluster of photosystem II. *Biochemistry* 53(18):2941–2955.
36. Taguchi Y, Noguchi T (2007) Drastic changes in the ligand structure of the oxygen-evolving Mn cluster upon Ca²⁺ depletion as revealed by FTIR difference spectroscopy. *Biochim Biophys Acta* 1767(6):535–540.
37. Kern J, et al. (2013) Simultaneous femtosecond X-ray spectroscopy and diffraction of photosystem II at room temperature. *Science* 340(6131):491–495.
38. Askerka M, Wang J, Brudvig GW, Batista VS (2014) Structural changes in the oxygen-evolving complex of photosystem II induced by the S₁ to S₂ transition: A combined XRD and QM/MM study. *Biochemistry* 53(44):6860–6862.
39. Debus RJ, Strickler MA, Walker LM, Hillier W (2005) No evidence from FTIR difference spectroscopy that aspartate-170 of the D1 polypeptide ligates a manganese ion that undergoes oxidation during the S₀ to S₁, S₁ to S₂, or S₂ to S₃ transitions in photosystem II. *Biochemistry* 44(5):1367–1374.
40. Strickler MA, Hillier W, Debus RJ (2006) No evidence from FTIR difference spectroscopy that glutamate-189 of the D1 polypeptide ligates a Mn ion that undergoes oxidation during the S₀ to S₁, S₁ to S₂, or S₂ to S₃ transitions in photosystem II. *Biochemistry* 45(29):8801–8811.
41. Strickler MA, Walker LM, Hillier W, Britt RD, Debus RJ (2007) No evidence from FTIR difference spectroscopy that aspartate-342 of the D1 polypeptide ligates a Mn that undergoes oxidation during the S₀ to S₁, S₁ to S₂, or S₂ to S₃ transitions in photosystem II. *Biochemistry* 46(11):3151–3160.
42. Service RJ, et al. (2013) Participation of glutamate-333 of the D1 polypeptide in the ligation of the Mn₄CaO₅ cluster in photosystem II. *Biochemistry* 52(47):8452–8464.
43. Pokhrel R, Service RJ, Debus RJ, Brudvig GW (2013) Mutation of lysine 317 in the D2 subunit of photosystem II alters chloride binding and proton transport. *Biochemistry* 52(28):4758–4773.
44. Suzuki H, et al. (2013) Functional roles of D2-Lys317 and the interacting chloride ion in the water oxidation reaction of photosystem II as revealed by fourier transform infrared analysis. *Biochemistry* 52(28):4748–4757.
45. Pokhrel R, Debus RJ, Brudvig GW (2015) Probing the effect of mutations of asparagine 181 in the D1 subunit of photosystem II. *Biochemistry* 54(8):1663–1672.
46. Service RJ, Hillier W, Debus RJ (2010) Evidence from FTIR difference spectroscopy of an extensive network of hydrogen bonds near the oxygen-evolving Mn₄Ca cluster of photosystem II involving D1-Glu65, D2-Glu312, and D1-Glu329. *Biochemistry* 49(31):6655–6669.
47. Service RJ, Hillier W, Debus RJ (2014) Network of hydrogen bonds near the oxygen-evolving Mn₄CaO₅ cluster of photosystem II probed with FTIR difference spectroscopy. *Biochemistry* 53(6):1001–1017.
48. Terrett R, Frankcombe T, Pace R, Stranger R (2016) Effect of concomitant oxidation and deprotonation of hydrated Mn centres in rationalising the FTIR difference silence of D1-Asp170 in Photosystem II. *J Inorg Biochem* 155:101–104.
49. Suzuki H, Sugiura M, Noguchi T (2009) Monitoring proton release during photosynthetic water oxidation in photosystem II by means of isotope-edited infrared spectroscopy. *J Am Chem Soc* 131(22):7849–7857.
50. Boussac A, Rutherford AW (1988) Nature of the inhibition of the oxygen-evolving enzyme of photosystem II induced by NaCl washing and reversed by the addition of Ca²⁺ or Sr²⁺. *Biochemistry* 27(9):3476–3483.
51. Vrettos JS, Stone DA, Brudvig GW (2001) Quantifying the ion selectivity of the Ca²⁺ site in photosystem II: Evidence for direct involvement of Ca²⁺ in O₂ formation. *Biochemistry* 40(26):7937–7945.
52. Pitari F, Bovi D, Narzi D, Guidoni L (2015) Characterization of the Sr²⁺- and Cd²⁺-substituted oxygen-evolving complex of photosystem II by quantum mechanics/molecular mechanics calculations. *Biochemistry* 54(38):5959–5968.
53. Yocum CF (1991) Calcium activation of photosynthetic water oxidation. *Biochim Biophys Acta* 1059(1):1–15.
54. Case D, et al. (2012) AMBER 12 (University of California, San Francisco).
55. Vreven T, et al. (2006) Combining quantum mechanics methods with molecular mechanics methods in ONIOM. *J Chem Theory Comput* 2(3):815–826.
56. Frisch MJ, et al. (2009) Gaussian 09, Revision C.01 (Gaussian, Inc., Wallingford, CT).